

Article

Control of the Boundary between the Gradual and Abrupt Modulation of Resistance in the Schottky Barrier Tunneling-Modulated Amorphous Indium-Gallium-Zinc-Oxide Memristors for Neuromorphic Computing

Jun Tae Jang [†], Geumho Ahn [†], Sung-Jin Choi, Dong Myong Kim and Dae Hwan Kim ^{*ID}

School of Electrical Engineering, Kookmin University, Seoul 02707, Korea; jtjang@kookmin.ac.kr (J.T.J.); 20113145@kookmin.ac.kr (G.A.); sjchoiee@kookmin.ac.kr (S.-J.C.); dmkim@kookmin.ac.kr (D.M.K.)

* Correspondence: drlife@kookmin.ac.kr; Tel.: +82-2-910-4872

[†] These authors are co-first author.

Received: 4 September 2019; Accepted: 23 September 2019; Published: 25 September 2019



Abstract: The transport and synaptic characteristics of the two-terminal Au/Ti/ amorphous Indium-Gallium-Zinc-Oxide (a-IGZO)/thin SiO₂/p⁺-Si memristors based on the modulation of the Schottky barrier (SB) between the resistive switching (RS) oxide layer and the metal electrodes are investigated by modulating the oxygen content in the a-IGZO film with the emphasis on the mechanism that determines the boundary of the abrupt/gradual RS. It is found that a bimodal distribution of the effective SB height (Φ_B) results from further reducing the top electrode voltage (V_{TE})-dependent Fermi-level (E_F) followed by the generation of ionized oxygen vacancies (V_O^{2+} s). Based on the proposed model, the influences of the readout voltage, the oxygen content, the number of consecutive V_{TE} sweeps on Φ_B , and the memristor current are explained. In particular, the process of V_O^{2+} generation followed by the Φ_B lowering is gradual because increasing the V_{TE} -dependent E_F lowering followed by the V_O^{2+} generation is self-limited by increasing the electron concentration-dependent E_F heightening. Furthermore, we propose three operation regimes: the readout, the potentiation in gradual RS, and the abrupt RS. Our results prove that the Au/Ti/a-IGZO/SiO₂/p⁺-Si memristors are promising for the monolithic integration of neuromorphic computing systems because the boundary between the gradual and abrupt RS can be controlled by modulating the SiO₂ thickness and IGZO work function.

Keywords: a-IGZO memristor; Schottky barrier tunneling; non filamentary resistive switching; gradual and abrupt modulation; bimodal distribution of effective Schottky barrier height; ionized oxygen vacancy

1. Introduction

The electronic computing systems developed so far have been structured on the von Neumann architecture in which the memory, the processor, and the controller exist separately, and the sequential processing among them embodies specific functions within the programmed software. Most of the digital and analog circuits included in the memory and processing units are composed of complementary metal-oxide-semiconductor (CMOS) devices that have made a significant contribution to the semiconductor industry. Improvements in the performance of modern computing and information technology are based on the permanent scaling down of the CMOS devices, which provide a cost-effective increase in the operating frequency and a reduction in the power consumption [1,2].

Currently, the integration density of CMOS devices do not conform to Moore's law [3], and the scaling down is fast approaching the physical limit. However, an increase in the operating frequency and the device density increases the power consumption and the operation temperature, which can seriously degrade the system performance (von Neumann bottleneck), mainly because of the time and energy spent in transporting data between the memory and the processor [4]. This is particularly noticeable for data-centric applications, such as real-time image recognition and natural language processing, where the state-of-the-art von Neumann systems cannot outperform an average human.

Unlike with the von Neumann systems, the human brain creates a massively parallel architecture by connecting a large number of low-power computing elements (neurons) and adaptive memory elements (synapses). Thus, the brain can outperform modern processors on many tasks that involve unstructured data classification and pattern recognition [5]. Furthermore, the ultra-dense crossbar array consisting of memristors have been recognized as a potentially promising path to building neuromorphic computing systems that can mimic the massive parallelism and extremely low-power operations found in the human brain [6]. Representative types of neuromorphic computing schemes are the biologically inspired spiking neural networks (SNNs) and deep neural networks, which are vector matrix multipliers [7,8]. The SNNs are based on the local spike-timing-dependent plasticity (STDP) learning rule [7], whereas the latter is based on the backpropagation learning rule [8].

The two-terminal binary metal-oxide-based resistive switching (RS) devices, such as HfO_x , AlO_x , WO_x , TaO_x , and TiO_x , have been widely studied as memristor devices that play the role of synapses in the crossbar arrays because the underlying metal–insulator–metal structure is simple, compact, CMOS-compatible, and highly scalable. Indeed, their energy consumptions per synaptic operation and programming currents can be made ultralow (sub-pJ energies, $<1 \mu\text{A}$ programming current) [9]. However, in most cases of these *filamentary* resistive switching random access memory (hereinafter ReRAM) devices, the filament formation/completion process is inherently abrupt and difficult to control. This problem is particularly acute in neuromorphic applications because a single highly conductive device with a thick filament provides much more current to a vector-weighted sum or a leaky integrate-and-fire than its neighbors [10]. Undoubtedly, the gradual RS characteristics (i.e., the analog nonvolatile memory characteristics of the memristors) are most viable for either the weighted sum operation of convolutional neural networks (CNNs) or the STDP as a learning rule for SNN. In particular, the synapse device using the memristor requires excellent linearity according to the consecutive potentiation/depression pulse for high data processing accuracy [11].

In the case of filamentary ReRAM devices, there is ambiguity at the boundary between the application of the digital memory device using the abrupt RS operation and the application of the synapse device using the gradual RS operation. Therefore, it is very difficult to optimize each of the devices for both applications in terms of the process and the material. More noticeably, the efficiency and linearity of the resistance modulations of the metal-oxide-based memristors are frequently contradictory to one another when applying the potentiation/depression (P/D) pulses [12]. This is because when the resistance changes of the filamentary ReRAM devices occur more efficiently (abruptly), the resistances become more nonlinear in relation to the increase in the number of P/D pulses. After being triggered by an electric field and/or a local temperature rise during the SET/potentiation pulse, the filament formation/completion must be cut by an external circuit so that the filament is not too thick to be removed with an accessible RESET/depression pulse. Despite using techniques such as incrementally increasing the amplitude of the P/D voltage and/or increasing the duration of the P/D pulse [13], the complicated scheme for self-adaptively varying either the amplitude or the duration of the P/D pulse would be significantly compromised with the use of external controls and circuits. This results in additional power consumption and design complexity and seriously dilutes the motivation of neuromorphic computing systems.

However, *non-filamentary* RS two-terminal devices based on binary metal-oxides have demonstrated more gradual (well-controlled, memristor-like) RS characteristics in comparison with filamentary RS devices [14] because the non-filamentary devices are based on the modulation of

the Schottky barrier (SB) between the RS oxide layer and the metal electrodes rather than the formation/rupture of the filament in the oxide layer.

Regardless of the type of RS devices, for a systematic and robust design of a self-adaptive P/D pulse scheme, it is important to have a complete understanding of the physical mechanism that controls the boundary of an abrupt/gradual RS characteristic. Therefore, it is important to understand the systematic design of the memristor devices for neuromorphic computing and precisely control the mechanism on the boundary of the abrupt and the gradual RS operations.

Quaternary metal-oxides, such as amorphous indium-gallium-zinc-oxide (a-IGZO), have more complicated compositions and they cannot be easily fabricated by low-temperature sputtering or the solution process. The a-IGZO materials can be fabricated on a flexible substrate and can act as both the RS and active films in memristors and thin-film transistors (TFTs), respectively [15–20]; this suggests that it is possible to monolithically integrate not only the synapse array but also the peripheral circuits including the neurons. In fact, two-terminal IGZO devices and their abrupt/gradual switching characteristics using metal electrodes, such as Pt, Al, and Cu, have already been demonstrated [16–20]. Even unipolar/bipolar IGZO memristor devices have been developed [19,20]. However, there is no known mechanism for determining the boundary of an abrupt/gradual RS in IGZO memristor devices.

In this study, we fabricated two-terminal Au/Ti/a-IGZO/thin SiO₂/p⁺-Si memristors and analyzed their transport and synaptic characteristics. Moreover, we investigated the mechanism determining the boundary of the abrupt/gradual RS by modulating the oxygen content in an a-IGZO film. Related to this mechanism, we also reported a bimodal distribution of effective Schottky barriers in a-IGZO non-filamentary ReRAM-based memristors.

2. Fabrication Process and Conduction Mechanism

To implement the synapse devices in bio-inspired neuromorphic computing systems (Figure 1a), we fabricated the two-terminal Au/Ti/IGZO/SiO₂/p⁺-Si memristors as shown Figure 1b. The p⁺-Si conductive substrate acts as a global bottom electrode (BE), and the 4-nm-thick SiO₂ was formed on the BE as the tunnel barrier in the interface between p⁺-Si and IGZO. Then, the 80-nm-thick a-IGZO film was deposited on SiO₂/p⁺-Si using radio frequency sputtering with a power of 150 W at room temperature. We controlled the concentration of oxygen vacancies (V_{OS}) during the IGZO sputtering by modulating the oxygen flow rates (OFR) to 1.0, 1.15, and 1.3 sccm at a fixed Ar flow rate of 3 sccm and at a constant gas pressure in the sputter chamber of 0.880 Pa. Subsequently, 10-nm-thick Ti was deposited using e-beam evaporation to form an oxygen reservoir layer and act as the top electrode (TE) of the memristor. Finally, the 40-nm-thick Au was deposited using e-beam evaporation to prevent the oxidation of the Ti layer in air.

To analyze the electrical characteristics, the DC current–voltage (I – V) characteristics were measured at room temperature and dark conditions using a Keithley-4200 semiconductor characterization system (Tektronix, Seoul, South Korea). In all the measurements, a voltage was applied to the TE, and the BE was always connected to the ground. The TE voltage was symbolized as V_{TE} , and the current flowing through the IGZO memristor was called I_{mem} , as shown in Figure 1b.

Figure 1c–f shows the energy band diagrams under various conditions: before forming the junction (Figure 1c), at the thermal equilibrium (Figure 1d), at a low V_{TE} (Figure 1e), and at a high V_{TE} (Figure 1f). Here, we considered the lowering of the height of the effective SB and denoted it as $q\Phi_B$ (eV). While SB lowering was insignificant at a thermal equilibrium, $q\Phi_B$ became low as the V_{TE} increased. At a low V_{TE} , most of the V_{TE} was applied across the thin SiO₂ layer (Figure 1e), whereas the increased V_{TE} was used mainly to deplete the IGZO film (Figure 1f). Energy band diagrams suggested the fabricated IGZO memristors operated as non-filamentary RS devices based on the SB modulation. The two main concerns were whether the modulated $q\Phi_B$ was nonvolatile and whether its decrease was inversely linear with the increase of V_{TE} . These two concerns will be discussed later.

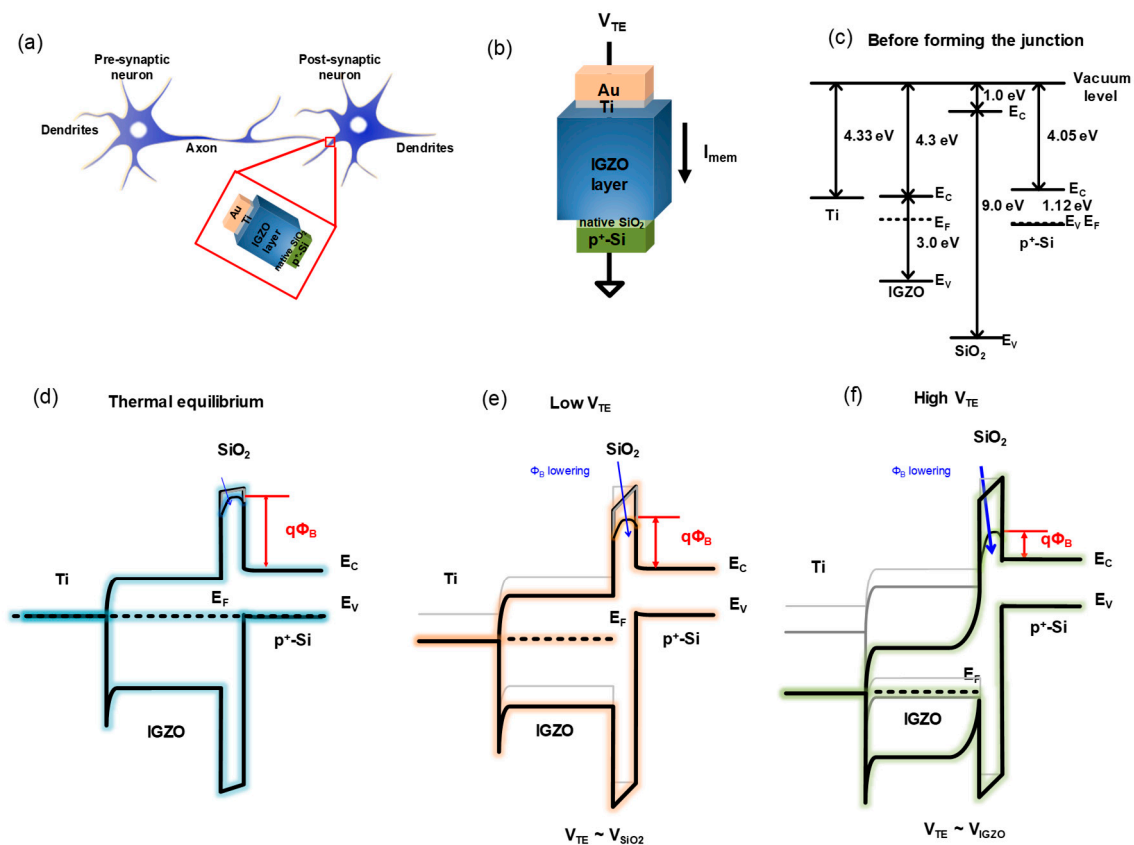


Figure 1. Schematic illustration of (a) the implementation of the synapse devices in bio-inspired neuromorphic computing systems and (b) the two-terminal Au/Ti/(amorphous indium-gallium-zinc-oxide) a-IGZO/SiO₂/p⁺-Si memristors. Energy band diagram (c) before forming the junction, and under three conditions: (d) in a thermal equilibrium, (e) at a low (top electrode voltage) V_{TE} , and (f) at a high V_{TE} .

We measured the OFR-dependent I_{mem} while using a positive V_{TE} sweep (SET process), that is, $0\text{ V} \rightarrow 6\text{ V} \rightarrow 0\text{ V}$ was repeated four times. Then, a negative V_{TE} sweep (RESET process), that is, $0\text{ V} \rightarrow -2\text{ V} \rightarrow 0\text{ V}$ was repeated four times, as shown in Figure 2a. We observed that the current at a fixed V_{TE} increased as the OFR decreased. This was attributed to the increase of the V_O concentration with the decrease in the OFR because the V_O is a well-known electron donor in the IGZO film [21,22]. Along with the SB-modulated non-filamentary RS devices in Figure 1e,f, a gradual resistance modulation rather than an abrupt RS was clearly observed during repeated $I-V$ sweeps (Figure 2a).

Figure 2b also shows the $I_{mem}-V_{TE}$ characteristic of the IGZO memristor with OFR = 1 sccm. In Figure 2b, the positive V_{TE} voltage sweep was repeated four consecutive times by changing the stop voltage of the V_{TE} sweep (V_{SS}) from 2 to 6 V. When the V_{TE} sweep was performed four times, the readout current I_{mem} at $V_{TE} = 1\text{ V}$ increased very slightly for $V_{SS} < 6\text{ V}$, as seen in Figure 2c. The continuous and hysteretic increase of current, which is a typical behavior of a memristor, is clearly observed in Figure 2a,b. There was a significant increase in I_{mem} only when $V_{SS} \geq 6\text{ V}$, which means that the *potentiation threshold* voltage between the gradual/abrupt RS (V_{PT}) was 6 V. Similarly, the *depression threshold* voltage was found to be -2 V .

To determine the conduction mechanism, we investigated the relationship between I_{mem} and V_{TE} . Figure 3a shows the OFR-dependent $\ln(I_{mem})$ versus $(V_{TE})^{1/2}$ relationships, which were taken from the $I-V$ characteristics of the first sweep in Figure 2a. In Figure 3a, we observed that the $\ln(I_{mem})$ was piecewise linear with $(V_{TE})^{1/2}$, which was strongly reminiscent of the thermionic emission. Noticeably, these linear relationships were clearly classified into two distinguishable values of the slopes A (at a low V_{TE}) and B (at a high V_{TE}).

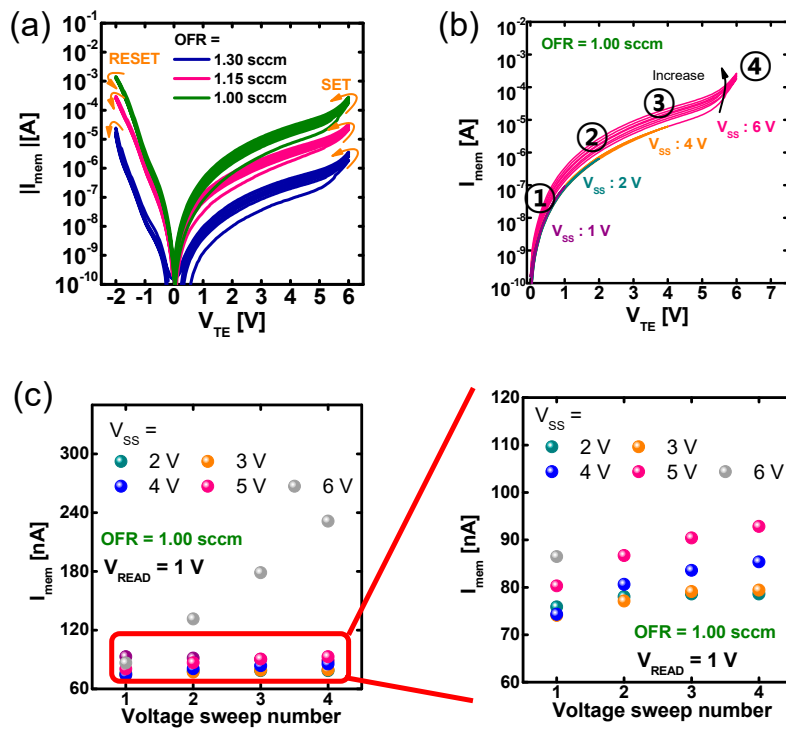


Figure 2. (a) The (oxygen flow rate) OFR-dependent $I-V$ characteristics repeated four times. (b) The $I-V$ characteristics with OFR = 1 sccm repeated four consecutive times with changes made to the (stop voltage of the V_{TE} sweep) V_{SS} . (c) The V_{SS} -dependent readout current I_{mem} at $V_{TE} = 1$ V.

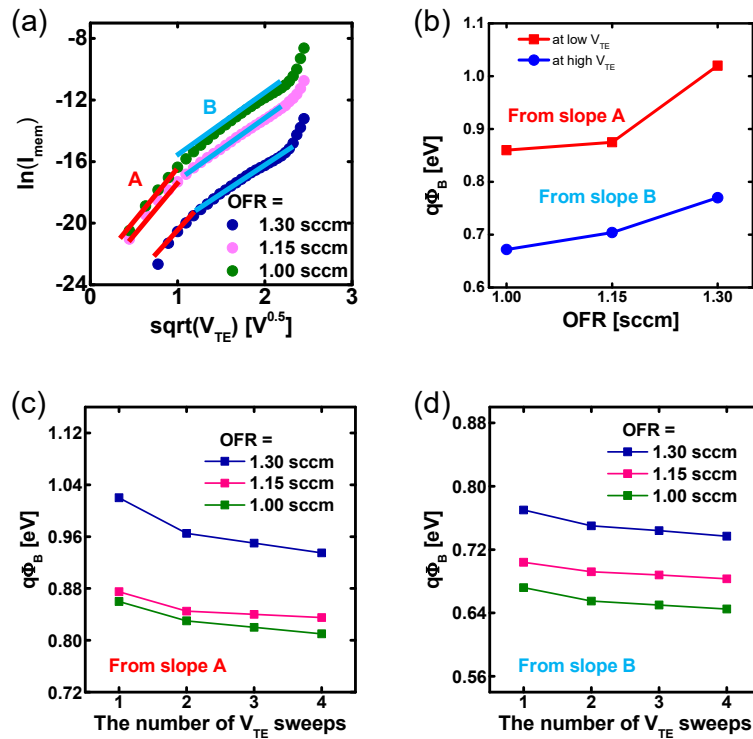


Figure 3. (a) The OFR-dependent $\ln(I_{mem})-(V_{TE})^{1/2}$ relationships. (b) The OFR-dependent Φ_B extracted at low and high V_{TE} . The Φ_B modulation depending on the number of V_{SS} from the slopes (c) A at high V_{TE} and (d) B at low V_{TE} .

The current due to the thermionic emission through SB is given as:

$$I_{\text{mem}} = AA^*T^2 \exp\left(\frac{q(\sqrt{qE/4\pi\epsilon} - \Phi_B)}{kT}\right) = AA^*T^2 \exp\left(\frac{q(\sqrt{qV_{\text{TE}}/4\pi\epsilon X_T} - \Phi_B)}{kT}\right) \quad (1)$$

where A is the area of device, A^* is the Richardson constant, T is the absolute temperature, k is Boltzmann's constant, E is the electric field; q is the electric charge, ϵ is the dielectric constant, X_T is the effective thickness of thermionic emission, and Φ_B is the effective SB height. Then, Equation (1) is used for extracting Φ_B . By reformulating from Equation (1) to (2), Φ_B can be extracted by using the y -intercept of the linear relationship between $\frac{kT}{q} \cdot \ln\left(\frac{I_{\text{mem}}}{AA^*T^2}\right)$ and $\sqrt{V_{\text{TE}}}$:

$$\frac{kT}{q} \cdot \ln\left(\frac{I_{\text{mem}}}{AA^*T^2}\right) = \sqrt{\frac{q}{4\pi\epsilon}} \times \sqrt{V_{\text{TE}}} - \Phi_B \quad (2)$$

Figure 3a,b suggests that at a specific OFR, there existed two Φ_B values taken from the slopes A and B, that is, a large value for a low V_{TE} (<1 V) and a small value for a high V_{TE} (1–5 V). Interestingly, we observed this bimodal distribution of Φ_B regardless of the OFR condition and suggest that the SB lowering is nonvolatile and significantly nonlinear with the increase in V_{TE} . In addition, Φ_B at a specific V_{TE} was lower because the V_{O} concentration increases (with decreasing OFR).

However, from Figure 2a, we can see that the Φ_B modulation depended on the number of positive V_{TE} sweeps (see Figure 3c,d). At a specific V_{TE} and OFR, Φ_B gradually decreased when the number of V_{SS} sweeps increased.

3. Results and Discussion

In Figure 3, we can see that Φ_B was modulated by not only the range of the V_{TE} readout voltage, but also by the number of consecutive V_{SS} sweeps. Moreover, as shown in Figure 3b,c, Φ_B depends more strongly on OFR in the slope A case (low V_{TE}) rather than in the slope B case (high V_{TE}). Therefore, the results in Figure 3 provide a clue toward the controllability of the competition between the gradual and abrupt modulations of Φ_B . To understand the mechanism for determining the boundary of an abrupt/gradual RS in IGZO memristor devices, we used Figure 3 with the energy band diagram.

First, when $V_{\text{TE}} < V_{\text{PT}}$, the bimodal distribution of Φ_B into A and B (Figure 3a) can be explained as follows. As shown in Figure 4a, the doubly ionized V_{O} (V_{O}^{2+}) is the well-known metastable state [21,22] and has been frequently pointed out as having a microscopic origin on the device instability under photo-illumination or bias stress [22–26] and persistent photoconductivity [25,26]. From the viewpoint of the subgap density of states (DOSs) in the a-IGZO (Figure 4b), the neutral V_{O} states (V_{O}^0 s) are transformed into V_{O} (V_{O}^{2+} s) when the process of $V_{\text{O}}^0 \rightarrow V_{\text{O}}^{2+} + 2e^-$ becomes energetically favorable. These neutral states are very slowly recovered (nonvolatile) [23–26].

In the readout voltage V_{TE} -dependent energy band diagrams, which are illustrated in Figure 4c, as V_{TE} increases, the Fermi-energy level (E_{F}) in IGZO reduces far from the IGZO conduction band minimum (E_{C}), and moves closer to the V_{O}^0 states above the IGZO valence band maximum (E_{V}). It makes the generation of V_{O}^{2+} s more energetically favorable. When V_{O}^{2+} s is generated, the concentration of the carrier electrons in E_{C} increases; the E_{F} in IGZO again comes closer to E_{C} . This situation occurs in non-equilibrium; therefore, the generation of V_{O}^{2+} s effectively makes Φ_B lower.

Thus, if the V_{O} ionization is nonvolatile, Φ_B would gradually decrease as the readout voltage V_{TE} increases. In other words, Φ_B has to be inversely linear to V_{TE} . However, Φ_B was classified into two groups (A and B), as seen in Figure 3. Figure 1e,f shows that a large Φ_B (in low V_{TE}) taken from the slope A corresponded to the voltage range where the maximum V_{TE} was applied across a thin SiO_2 layer (Figure 1e), whereas a small Φ_B (in high V_{TE}) taken from the slope B corresponded to the voltage range where the maximum increase in V_{TE} was mainly applied across the IGZO film (Figure 1f). Then, there would be a significant generation of V_{O}^{2+} s only in the latter range (Figure 4c). In Figure 2c, I_{mem} gradually increased only when V_{TE} was in the latter range, that is, in the range $2 \text{ V} \leq V_{\text{TE}} < V_{\text{PT}}$.

Our discussion indicates that the bimodal distribution of Φ_B in IGZO memristors originated from the generation of metastable V_O^{2+} states.

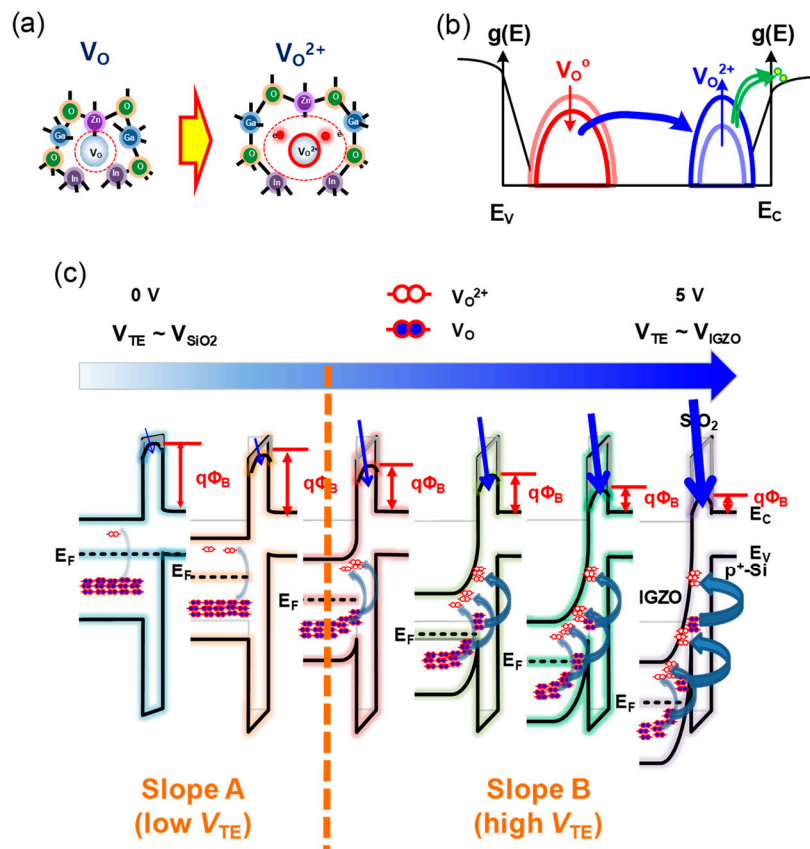


Figure 4. Schematic illustration of oxygen vacancies ionization from the viewpoint of (a) the atomic structures and (b) the subgap DOS in a-IGZO. (c) The read voltage V_{TE} -dependent energy band diagram.

Next, we investigated the OFR-dependence of Φ_B . Figure 5a–c illustrates the energy band diagram of the device fabricated with a high OFR (O-rich device) under three conditions: at a thermal equilibrium (Figure 5a), at a low V_{TE} (Figure 5b), and at a high V_{TE} (Figure 5c). Figure 5d–f illustrates the energy band diagram of the device fabricated using a low OFR (O-poor device) in three states: at a thermal equilibrium (Figure 5d), at a low V_{TE} (Figure 5e), and at a high V_{TE} (Figure 5f). As seen in Figure 5a,d, a larger amount of V_O^0 s existed in the IGZO when the OFR decreased from 1.3 to 1.0 sccm. Then, as the IGZO was O-poorer, the IGZO work function decreased, and Φ_B became lower, which is consistent with Figure 3b. In addition, as mentioned in Figure 3b,c, the OFR-dependence of Φ_B was larger in the slope A case (low V_{TE}) rather than in the slope B case (high V_{TE}). The Φ_B before the V_O^{2+} generation (at a low V_{TE}) was determined mainly by the OFR condition. After a significant amount of V_O^{2+} s were generated at a high V_{TE} , the initial OFR-dependence of Φ_B was combined with the V_{TE} -dependence of Φ_B . Thus, the OFR-dependence of Φ_B was diluted in the slope B case (high V_{TE}).

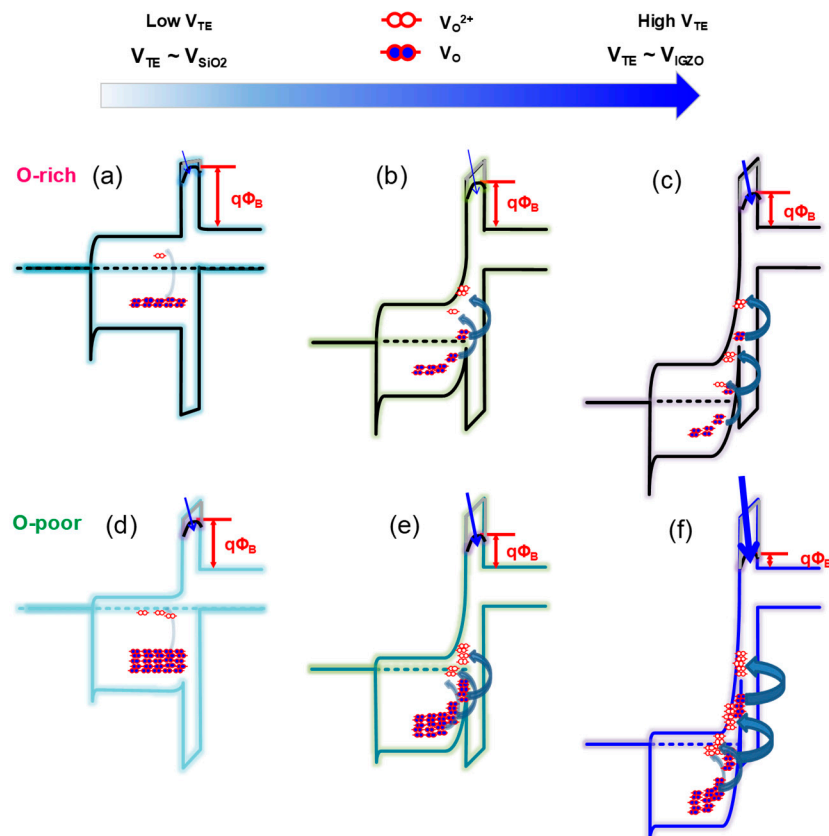


Figure 5. The OFR-dependent energy band diagram and Φ_B with (a)–(c) high OFR and (d)–(f) low OFR at (a,d) thermal equilibrium, (b,e) low V_{TE} , and (c,f) high V_{TE} .

Finally, the evolution of Φ_B with the increase in the number of consecutive positive V_{SS} sweeps is illustrated in the energy band diagrams in Figure 6. When the V_{SS} sweeps were repeated four times, Φ_B gradually decreased because of the gradual increase in V_{O}^{2+} s. However, the process of V_{O}^{2+} generation followed by Φ_B lowering was not abrupt; it was gradual because further lowering of the V_{TE} -dependent E_F followed by the V_{O}^{2+} generation was self-limited due to the increasing of the electron concentration–dependent E_F . The results in Figure 3c,d explain this well. If $V_{TE} \geq V_{PT}$, the change of I_{mem} becomes abrupt because E_F is aligned with the level of the V_{O}^0 s peak in DOS (Figure 4b).

Therefore, we can classify the operation regime in the two-terminal Au/Ti/a-IGZO/SiO₂/p⁺-Si memristors into three parts: (1) low V_{TE} ($V_{TE} < 2$ V), (2) high V_{TE} (2 V $\leq V_{TE} \leq V_{PT}$), and (3) higher V_{TE} ($V_{TE} \geq V_{PT}$). The boundary between (1) and (2) was approximately 2 V in our case; it was determined by the process/structure details and was controllable using the SiO₂ thickness and the IGZO work function. The V_{TE} in regime (1) was adequate for the readout voltage because Φ_B and I_{mem} were determined mainly by the OFR condition. However, the V_{TE} in regime (2) can be used as the amplitude of the potential pulse because Φ_B and I_{mem} gradually change in a nonvolatile manner with the increase in the number of consecutive V_{SS} sweeps. When the V_{TE} in regime (3) was applied to the devices, they operated as abrupt RS switches rather than as gradual RS memristors.

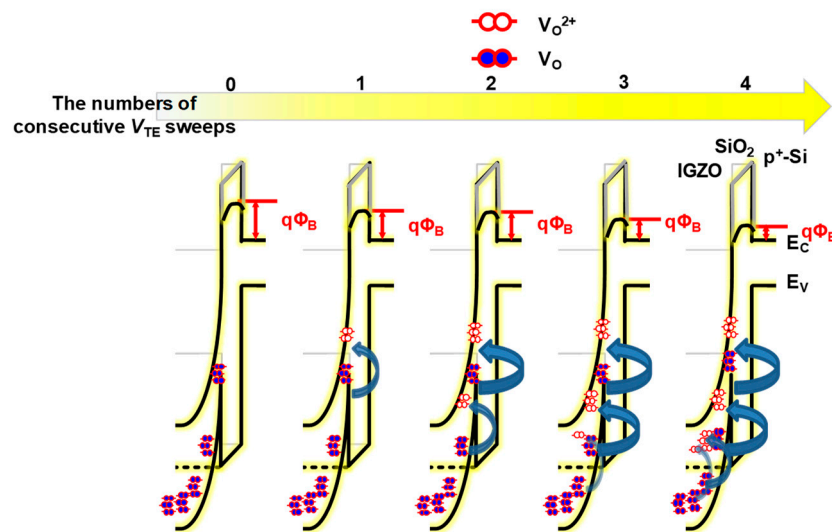


Figure 6. Energy band diagram for the evolution of Φ_B with the increase in the number of consecutive positive V_{SS} sweeps.

4. Conclusions

It is crucial to have good control over the mechanism on the boundary between the abrupt and gradual RS operations for a systematic design of memristor devices for neuromorphic computing. We investigated the transport and synaptic characteristics of two-terminal Au/Ti/a-IGZO/thin SiO₂/p⁺-Si memristors by varying the oxygen content in the a-IGZO film by emphasizing the mechanism determining the boundary of the abrupt/gradual RS. A bimodal distribution of Φ_B was produced to further lower the V_{TE} -dependent E_F followed by the generation of V_O^{2+} s. Based on the proposed model, we explained the influence of the readout voltage, the oxygen content, and the number of consecutive V_{SS} sweeps on Φ_B and I_{mem} . Eventually, we proposed three operation regimes: the readout, the potentiation in gradual RS, and the abrupt RS.

Our results prove that the Au/Ti/a-IGZO/SiO₂/p⁺-Si memristors are promising for the monolithic integration of neuromorphic computing systems because the boundary between the gradual and the abrupt RS can be controlled by modulating the SiO₂ thickness and the IGZO work function. Furthermore, the memristors are expected to be potentially useful for the co-design and joint optimization of the IGZO memristors and TFTs for neuromorphic energy-efficient wearable healthcare circuits and systems.

Author Contributions: The manuscript was prepared by J.T.J., G.A., S.-J.C., D.M.K., and D.H.K. Device fabrication was performed by J.T.J. and G.A. Results and discussion were performed by J.T.J., G.A., and D.H.K.

Funding: This work was supported by the national research foundation (NRF) of Korea funded by the Korean government under Grant 2016R1A5A1012966, 2016M3A7B4909668, 2017R1A2B4006982, and in part by an Electronics and Telecommunications Research Institute (ETRI) grant funded by the Korean government (18ZB1800).

Conflicts of Interest: The authors declare no conflict of interest.

References

1. Wan, Q.; Sharbati, M.T.; Erickson, J.R.; Du, Y.; Xiong, F. Emerging Artificial Synaptic Device for Neuromorphic Computing. *Adv. Mater. Technol.* **2019**, *4*, 1900037. [[CrossRef](#)]
2. Upadhyay, N.K.; Jiang, H.; Wang, Z.; Asapu, S.; Xia, Q.; Yang, J.J. Emerging Memory Devices for Neuromorphic Computing. *Adv. Mater. Technol.* **2019**, *4*, 1800589. [[CrossRef](#)]
3. Kish, L.B. End of Moore's law: Thermal (noise) death of integration in micro and nano electronics. *Phys. Lett. A* **2002**, *305*, 144–149. [[CrossRef](#)]
4. Neumann, J.V. First Draft of a Report on the EDVAC. *Ann. Hist. Comput.* **1993**, *15*, 27–75. [[CrossRef](#)]

5. Indiveri, G.; Liu, S.-C. Memory and Information Processing in Neuromorphic Systems. *Proc. IEEE* **2015**, *103*, 1379–1397. [[CrossRef](#)]
6. Park, S.; Kim, H.; Choo, M.; Noh, J.; Sheri, A.; Jung, S.; Seo, K.; Park, J.; Kim, S.; Lee, W.; et al. RRAM-based Synapse for Neuromorphic System with Pattern Recognition Function. In Proceedings of the 2012 International Electron Devices Meeting, San Francisco, CA, USA, 10–13 December 2012; pp. 10.2.1–10.2.4.
7. Kheradpisheh, S.R.; Ganjtabesh, M.; Thorpe, S.J.; Masquelier, T. STDP-based spiking deep convolutional neural networks for object recognition. *Neural Netw.* **2018**, *99*, 56–67. [[CrossRef](#)] [[PubMed](#)]
8. LeCun, Y.; Bengio, Y.; Hinton, G. Deep learning. *Nature* **2015**, *521*, 436–444. [[CrossRef](#)] [[PubMed](#)]
9. Yu, S.; Gao, B.; Fang, Z.; Yu, H.; Kang, J.; Wong, H.-S.P. A Neuromorphic Visual System Using RRAM Synaptic Devices with Sub-pJ Energy and Tolerance to Variability: Experimental Characterization and Large-Scale Modeling. In Proceedings of the 2012 International Electron Devices Meeting, San Francisco, CA, USA, 10–13 December 2012; pp. 10.4.1–10.4.4.
10. Burr, G.W.; Shelby, R.M.; Sebastian, A.; Kim, S.; Kim, S.; Sidler, S.; Virwani, K.; Ishii, M.; Narayanan, P.; Fumarola, A. Neuromorphic computing using non-volatile memory. *Adv. Phys. X* **2016**, *2*, 89–124. [[CrossRef](#)]
11. Yu, S. Neuro-Inspired Computing with Emerging Nonvolatile Memory. *Proc. IEEE* **2018**, *106*, 260–285. [[CrossRef](#)]
12. Kim, S.; Choi, B.; Lim, M.; Yoon, J.; Lee, J.; Kim, H.-D.; Choi, S.-J. Pattern Recognition Using Carbon Nanotube Synaptic Transistors with an Adjustable Weight Update Protocol. *ACS Nano*. **2017**, *11*, 2814–2822. [[CrossRef](#)]
13. Jerry, M.; Chen, P.-Y.; Zhang, J.; Sharma, P.; Ni, K.; Yu, S.; Datta, S. Ferroelectric FET Analog Synapse for Acceleration of Deep Neural Network Training. In Proceedings of the 2017 International Electron Devices Meeting, San Francisco, CA, USA, 2–6 December 2017; pp. 6.2.1–6.2.4.
14. Woo, J.; Moon, K.; Song, J.; Lee, S.; Kwak, M.; Park, J.; Hwang, H. Improved Synaptic Behavior Under Identical Pulses Using AlO_x/HfO₂ Bilayer RRAM Array for Neuromorphic Systems. *IEEE Electron Device Lett.* **2016**, *37*, 994–997. [[CrossRef](#)]
15. Boldman, W.L.; Zhang, C.; Ward, T.Z.; Briggs, D.P.; Srijanto, B.R.; Brisk, P.; Rack, P.D. Programmable Electrofluidics for Ionic Liquid Based Neuromorphic Platform. *Micromachines* **2019**, *10*, 478. [[CrossRef](#)] [[PubMed](#)]
16. Dang, B.; Liu, K.; Zhu, J.; Xu, L.; Zhang, T.; Cheng, C.; Wang, H.; Yang, Y.; Hao, Y.; Huang, R. Stochastic neuron based on IGZO Schottky diodes for neuromorphic computing. *APL Mater.* **2019**, *7*, 071114. [[CrossRef](#)]
17. Wang, Z.Q.; Xu, H.Y.; Li, X.H.; Yu, H.; Liu, Y.C.; Zhu, X.J. Synaptic Learning and Memory Functions Achieved Using Oxygen Ion Migration/Diffusion in an Amorphous InGaZnO Memristor. *Adv. Funct. Mater.* **2012**, *22*, 2759–2765. [[CrossRef](#)]
18. Kado, K.; Uenuma, M.; Sharma, K.; Yamazaki, H.; Urakawa, S.; Ishikawa, Y.; Uraoka, Y. Thermal analysis for observing conductive filaments in amorphous InGaZnO thin film resistive switching memory. *Appl. Phys. Lett.* **2014**, *105*, 123506. [[CrossRef](#)]
19. Hu, W.; Zou, L.; Chen, X.; Qin, N.; Li, S.; Bao, D. Highly Uniform Resistive Switching Properties of Amorphous InGaZnO Thin Films Prepared by a Low Temperature Photochemical Solution Deposition Method. *ACS Appl. Mater. Interfaces* **2014**, *6*, 5012–5017. [[CrossRef](#)]
20. Wang, Z.; Xu, H.; Zhao, X.; Lin, Y.; Zhang, L.; Ma, J.; Liu, Y. Effect of reset voltage polarity on the resistive switching region of unipolar memory. *Phys. Status Solidi A* **2015**, *212*, 2255–2261. [[CrossRef](#)]
21. Janotti, A.; Van de Walle, C.G. Native point defects in ZnO. *Phys. Rev. B* **2007**, *76*, 165202. [[CrossRef](#)]
22. Migliorato, P.; Chowdhury, M.D.H.; Um, J.G.; Seok, M.; Jang, J. Light/negative bias stress instabilities in indium gallium zinc oxide thin film transistors explained by creation of a double donor. *Appl. Phys. Lett.* **2010**, *97*, 022108. [[CrossRef](#)]
23. Jang, J.T.; Park, J.; Ahn, B.D.; Kim, D.M.; Choi, S.-J.; Kim, H.-S.; Kim, D.H. Effect of direct current sputtering power on the behavior of amorphous indium-gallium-zinc-oxide thin-film transistors under negative bias illumination stress: A combination of experimental analyses and device simulation. *Appl. Phys. Lett.* **2015**, *106*, 123505. [[CrossRef](#)]
24. Hoshino, K.; Wager, J. Negative bias illumination stress assessment of indium gallium zinc oxide thin-film transistors. *J. Soc. Inf. Disp.* **2015**, *23*, 187–195. [[CrossRef](#)]

25. Jang, J.T.; Park, J.; Ahn, B.D.; Kim, D.M.; Choi, S.-J.; Kim, H.-S.; Kim, D.H. Study on the Photoresponse of Amorphous In–Ga–Zn–O and Zinc Oxynitride Semiconductor Devices by the Extraction of Sub-Gap-State Distribution and Device Simulation. *ACS Appl. Mater. Interfaces* **2015**, *7*, 15570–15577. [[CrossRef](#)] [[PubMed](#)]
26. Jeon, S.; Ahn, S.-E.; Song, I.; Kim, C.J.; Chung, U.-I.; Lee, E.; Yoo, I.; Nathan, A.; Lee, S.; Robertson, J.; et al. Gated three-terminal device architecture to eliminate persistent photoconductivity in oxide semiconductor photosensor arrays. *Nat. Mater.* **2012**, *11*, 301–305. [[CrossRef](#)] [[PubMed](#)]



© 2019 by the authors. Licensee MDPI, Basel, Switzerland. This article is an open access article distributed under the terms and conditions of the Creative Commons Attribution (CC BY) license (<http://creativecommons.org/licenses/by/4.0/>).